To be published in
IEEE Trans. on Nucl. Sci.

Presented at 1974 Nuclear Science
Symposium & 14th Scintillation &
Semiconductor Counter Symposium,
Washington, D. C., Dec. 11-13, 1974.

BNL 19487

Conf-741213--11
Conf-741212--11

A TWO-DIMENSIONAL POSITION-SENSITIVE DETECTOR FOR THERMAL NEUTRONS*

J. Alberi, J. Fischer, V. Radeka,
L. C. Rogers and B. Schoenborn

Brookhaven National Laboratory
Upton, New York 11973

December 1974

*This work was performed under the auspices of the
U. S. Atomic Energy Commission.

A TWO-DIMENSIONAL POSITION-SENSITIVE DETECTOR FOR THERMAL NEUTRONS*

J. Alberi, J. Fischer, V. Radeka,
L. C. Rogers and B. Schoenborn

Brookhaven National Laboratory
Upton, New York 11973

ABSTRACT

We have developed and tested a thermal neutron, two-dimensional position-sensitive detector for use in neutron scattering from biological samples. The detector is based on a multi-wire proportional concept with a gas filling of 6 atmos. He^3, 4 atmos. A, and 0.5 atmos. CO_2. The position readout uses a resistive wire with charge division to determine position. We have measured a resolution of less than 3 mm (FWHM) with a detection efficiency of 70% at 2.8 Å neutrons. Considerations leading to an optimal configuration are discussed.

1. Introduction

Position-sensitive detector systems for neutron scattering are a continuing need in neutron diffraction experiments.[1] Many possibilities suggest themselves as the method best suited to fulfill this need. Of these methods, we believe that gas discharge detection of neutron-induced charged particle reactions is the method of choice under existing technology for the detection of thermal neutrons. Of the possible types of gas discharge chambers, practical considerations, such as gamma ray background discrimination and count rate capacity, limit consideration of a practical detector to two types of chamber (a) ionization (non-multiplicative) and (b) proportional (multiplicative). Of the two types of chamber, we have chosen the proportional due to larger signal-producing capacity coupled with sufficient energy resolution.† The former attribute reduces the burden on the position sensing system while the latter enables the rejection of background gamma rays. Table I lists three charged particle reactions that are suitable for use in a gas discharge chamber to detect thermal neutrons. Of the three, only He^3 and B^{10} in the form of BF_3 are of practical use. The $He^3(n,p)T$ reaction has a reaction energy of 764 keV and a cross section of 5327 barns. The $B^{10}(n,\alpha)Li^7$ reaction has a reaction energy of 2.79 MeV and a cross section of 3840 barns.[5] We have chosen the former due to its ability to operate at high pressures and relatively low voltages with good multiplication and to its high thermal neutron cross section.[6,7,8,9] The relatively low reaction energy is not a liability since there is sufficient gas gain available in the chamber. There are several methods in use today of reading the position of the neutron induced reaction from the chamber.[10-18,27] Primary among these methods are (a) one amplifier-discriminator per wire; (b) delay line position sensing (whether dc coupled or capacitively coupled); (c) resistive wire (whether charge division or diffusive RC delay lines). The method of charge division of signals from a resistive wire readout is particularly suited to high pressure proportional chambers where signal rise times are slow. Non-dispersive delay lines do not offer sufficient delay per unit length to give adequate spatial resolution with the poor time resolution inherent in such slow rise signals. Even if such delay lines were available, the count rate capability of such a system would suffer due to the long event-processing time. The count rate capacity of the charge division readout is comparable to the charge collection time in a high pressure detector, and is sufficient to the needs of neutron diffraction studies at an economical cost. Charge division is understood theoretically, and the realization of a sufficiently fast divider is feasible as we shall demonstrate below. Hence, we have adopted this method as the basis for position readout in our detector.

Herein, we report the development of a neutron-sensitive, position-sensitive detector based on a ten-atmosphere, He^3 and A-filled, multiwire proportional chamber with resistive wire readout. Such a counter yields basic parameters of 70% neutron efficiency at 2.8 Å neutron-wavelength and 3 mm useful spatial resolution at FWHM along the coordinate parallel to the anode wires. The orthogonal coordinate is spatially quantized by the anode wires.

2. Detector

Figure 1 shows a schematic diagram of the multiwire proportional chamber geometry. The basic configuration consists of three wire planes with the anode at the center and two cathodes, one above and one below the anode. Each electrode is supported by a separate glass frame whose interior dimensions are 18.5 cm (7.3 in.) square. Thus the sensitive region of the chamber measures approximately 18 cm x 18 cm. Glass is used as the support of each electrode to reduce the possibility of contamination of the gases by outgassing of electronegative materials. In a closed system, over a long period of time, such outgassing could poison the chamber to the extent of rendering electron collection and gas multiplication impossible. Glass frames also have the advantage of reducing the hydrogenated materials in the chamber to a minimum; hence the sensitivity to any fast neutron flux component is minimized. The wires were wound on the frames by conventional winding techniques. The anode consists of 20 μm (0.0008 in.) diameter stainless steel wire with a spacing between wires of 2.54 mm (0.1 in.). Each cathode was fabricated of 100 μm (0.004 in.) diameter wire attached in the zig-zag fashion shown in

*This work was performed under the auspices of the U. S. Atomic Energy Commission.

†There exist several classical texts on gas discharge radiation detectors. We list some as Refs. (2), (3), (4).

Fig. 1(a).[19] Thus each cathode forms one long resistive readout wire with a total resistance of approximately 3000 ohms. The spacing between each readout wire is 1.27 mm. (0.05 in.). The use of a single, long resistive wire for readout simplifies the construction procedures used in this chamber, and, as we shall show later, the relatively low resistance does not adversely affect the position resolution of the chamber. Interelectrode spacing is 3.18 mm. (0.125 in.) and there is an additional 3.18 mm. between the cathode planes and the grounded surface of the pressure vessel. Charge from He^3 reaction product ionization is drifted into the interplane region from the drift space (Fig. 1b) by an electric field equivalent to that between the cathode-anode planes.

The three planes are assembled, as shown in Fig. 1a, and placed in an aluminum container capable of withstanding overpressures of 150 psig. Small gaps between the frames supporting the three electrodes were filled with a silicone rubber compound to prevent the high electric fields associated with edge breakdown. The entrance window of the pressure container is 0.95 cm (0.375 in.) thick and matched to the active area of the chamber. With this window, 8% of the incident neutrons are scattered out of the beam, assuming a scattering cross section of 1.46 barns for aluminum at thermal energy. Since the scattering is isotropic, approximately one half of the scattered neutrons will be detected in the counter, increasing the background. In general, the effect of this scatter is to produce broader non-gaussian tails to the position resolution function.

The gas used in filling the chamber must be of exceptionally high purity to yield good results at pressures of 10 atmospheres. High impurity levels, especially of water and oxygen, can cause electron trapping with consequent degradation in charge collection. The argon and carbon dioxide are batch analyzed by the manufacturer and found to have the following impurities: argon, $O_2 < 0.5$ ppm, $N_2 < 1$ ppm, dew point -105°F, and total hydrocarbons < 0.5 ppm; carbon dioxide, $O_2 < 0.5$ppm, $N_2 < 5.6$ ppm, dew point -130°F and total hydrocarbons < 0.5 ppm. The He^3, as supplied by the manufacturer, contains 10^3 ppm of unknown impurities. To remove the electronegative fraction of these, the helium is heated to 600°C in a calcium loaded purifier and held for 30 minutes.[20] After cooling, the gas is inserted into the detector without any further purification. The chamber was filled with 6 atmos. He^3, 4 atmos. A, and 0.5 atmos. CO_2. Energy spectra obtained with the detector with this gas mixture are consistent with those shown in Refs. (6-9) and, hence we conclude the gas is sufficiently pure for our application.

Outgassing of electronegative materials and leaks of noble gases at high preasures are always difficult problems when attempting to develop a high pressure, non-flowing gas proportional detector. We have measured the leak rate of our detector with a helium leak detector to be 5×10^{-6} std. cc/sec. Thus we should lose approximately 0.25% of the filling gas/month. Chamber outgassing limits the useful life of the gas to approximately 4 months between refillings. We are presently developing a "getter" type purifier on the detector to extend this time.

3. Neutron Detection Efficiency, Product Particle Range and Position Resolution Function

Unlike He^3 detectors without position sensitivity, where the range of the charged particles is unimportant (except to the extent that wall and end effects become important), position sensitive detectors require that the particles be stopped within the desired spatial resolution of the chamber.[21] Unfortunately He^3 by itself is not sufficiently dense at reasonable working pressure to stop the proton from the $He^3(n,p)H^3$ reaction in a reasonable distance. At 10 atmospheres the range of a 573 keV proton in He^3 is 1.045 mg/cm^2 or approximately 7.9 mm.[22] The H^3 ion range is approximately one-half that of the proton. Hence the proton range dominates. Thus there is an obvious need for a gas whose function is to stop the charged particles resulting from the detection reaction. We have conflicting requirements on gas composition which must be resolved, i.e., a high percentage of He^3 for detection efficiency vs. a high percentage of some denser gas for increased charged particle stopping-power. Increasing the working pressure of the chamber is a partial solution to this problem. However, mechanical limitations of the pressure vessel as well as charge collection and multiplication at high pressures in large chambers limit the pressure to approximately 10 atmospheres. A reasonable compromise of these factors is thus necessary to obtain performance characteristics that are satisfactory for small angle neutron diffraction scattering experiments.

Argon, a gas whose electron transport and multiplication properties are well known, has been chosen for the stopping gas in the detector.[2,3,4] In choosing a dense gas to stop the He^3 reaction products, the gamma-ray sensitivity of the detector, which arises from different detector elements at different incident energy, must also be considered. However, upon noting that the dependence on the atomic number, Z, of the photoelectric cross section is $Z^{4.5}$, of the Compton cross section is Z, and of the proton range is $Z^{-\frac{1}{2}}$, we have concluded that argon is preferable to denser noble gasses.[22,23] At gamma-ray energies below 200 keV, where most interactions are in the detector gas, argon has low photoelectric and Compton cross sections. At higher energy (1 MeV), where most detected gamma-ray events are caused by electrons recoiling from the detector walls, the ionization from the electron is higher in heavier gases, causing more measured charge.

Figure 2 shows calculated detector efficiency vs. neutron wavelength for a gas filling of 40% argon and 60% He^3 by volume at 10 atmospheres. The efficiency for 4 Å neutrons is 91%, and for 1.82 Å neutrons (thermal) is 67%. These efficiencies are more than sufficient for our application in biological neutron scattering. Figure 3 shows detection efficiency of 4 Å neutron vs. gas composition at 10 atmospheres pressure (curve A) and proton range vs. gas composition at 10 atmospheres pressure for two gases, argon and krypton, (curves B and C). The calculated value for proton range under the operating characteristics of the chamber (6 atmospheres He^3, 4 atmospheres A, 0.5 atmosphere CO_2) yields a proton range from the $He^3(n,p)H^3$ reaction of 2.3 mm. The accuracy of this figure is difficult to assess due to the lack of primary data.[22] However, we shall compare it to our observed spatial resolution in a later section.

From the above, it becomes possible to calculate the spatial resolution function for the proton and triton produced from the He^3 reaction. If we examine the paths of the charged particles emitted from a small volume of space ΔV in which neutrons are captured, it is clear from the kinetics that the proton and triton are emitted back to back and the direction of proton emission is isotropic. The proton, whose energy is 573 keV, has a range ~ 2 times as great as the triton, whose energy is 191 keV. Thus for neutrons captured in any small volume of space ΔV, the resultant ionization from many such captures will form a spherically symmetric distribution about the capture point. The radial dependence of the ionization

distribution will be complicated by the multiparticle emission and the spatially non-uniform specific ionization from these particles. We may, however, write a general expression for the spatial resolution function projected to one dimension, D(p), caused by this ionization cloud. In general,

$$D(p) = 2\pi \int_0^\infty \int_0^\pi r^2 \, dr \sin\theta \, d\theta \quad f(r)\delta(p - r\cos\theta) \quad (1)$$

where p = the spatial coordinate,

f(r) = the function describing the radial dependence of specific ionization caused by the proton and triton,

r,θ = variables of integration,

δ = Dirac δ-function.

The integral sums ionization over planes parallel to the x and y axis and at distance p above the origin. This formula may be further simplified by performing the integration over θ. Namely,

$$D(p) = 2\pi \int_p^\infty r \, dr \, f(r) \quad . \quad (2)$$

If one makes the simplifying assumption that f(r) is a uniform function of r with value φ up to some cut-off value R, the resolution function becomes

$$D(p) = \pi \phi (R^2 - p^2), \quad R \geq p \geq -R \quad . \quad (3)$$

One may calculate the full width at one half maximum (FWHM) of this distribution to be $\sqrt{2}$ R. If R is taken as the range of the proton, R_p, the predicted spatial resolution of the detector is 3.25 mm.

A more detailed calculation can be made using tabulated electronic stopping data.[22] From this data, a specific ionization distribution f(r) may be calculated numerically. The ionization function f(r) is derived from a superposition of ionization caused by the proton and triton reaction products from $He^3(n,p)H^3$. Figure 4 shows the one dimensional spatial resolution function, D(p), under two conditions: curve A, uniform ionization up to a cut-off range R_p, the proton range, and curve B, specific ionization derived from Bragg ionization curves. The FWHM of curve B is 1.2 x R_p and predicts a physical spatial resolution of 2.76 mm FWHM. This value agrees more closely with our experimental result.

The range of the reaction products has a small effect on detector efficiency for neutrons. A simple calculation shows that 10% of the protons and 5% of the tritons strike the detector wall before reaching the end of their range. The charge collected from these events is reduced, and depending on the charge threshold for valid events, the effective neutron sensitivity is also somewhat reduced.

4. Electric Fields in the Detector

We will now compute the electric field and interelectrode capacitance of the various elements of the detector (Fig. 1b). The field distribution must be known so that the charge transport in the drift space, charge multiplication and quantity of charge induced on the cathodes can be known for each event.

The electric field for the configuration shown in Fig. 1(a),(b) is difficult to calculate exactly. Charpak has given an exact field calculation in two dimensions for the simpler case of a wire grid between two grounded plane electrodes.[24] The exact solution for the configuration in Ref. (24) is closely approximated by formulae for a plane triode given in Spangenberg.[25] This approximate expression is valid when the interelectrode gap is greater than the wire spacing, and it can be written in the form,

$$V \sim q \left[2\pi L/s - \ln\left\{ 4 \sin^2(\pi x/s) + 4 \sinh^2(\pi y/s) \right\} \right] \quad (4)$$

$$q \sim \frac{V_o}{2[(\pi L/s - \ln \pi d/s)]} \quad (5)$$

where q is the charge/unit length on the wire

L is the interelectrode spacing (Fig. 1b)

s is the interwire spacing

x,y are coordinates

V_o is the potential applied to the central wire grid.

From this formula it is clear that the chamber has a region close to the wire in which the field falls as 1/r, (r<0.1s). Further away the field becomes uniform.

The capacitance of the central wire grid then becomes:

$$C = \varepsilon \frac{D^2}{2s} \frac{1}{[(\pi L/s - \ln \pi d/s)]} \quad (6)$$

where D is the length of one side of a square grid, C is the capacitance. This approximate form satisfies Poisson's equation. However, the equipotentials are only approximately circles at the central grid and straight lines at the ground planes under the conditions given above. Such an approximation is, however, quite adequate for our purpose. The more complex geometry of this detector, shown in Fig. 1(b), may be analyzed using functions based on the form given in Eq. (4). We have calculated the potential for cathode and anode wires running parallel, since crossed wires lead to a three-dimensional problem. Only this half of the chamber is then described in the calculation. Electrical characteristic should not be appreciably different in the other half. We assume the pressure vessel is the reference potential (ground). The cathodes are distance L_2 from the pressure vessel, have interwire spacing S_c, wire diameter d_c and charge q_c on each wire. The anode is at distance L_1 from the cathode, has wire spacing S_a, wire diameter d_a and charge q_a on each wire; q_b is the charge on the ground planes. With these definitions we may write the potential, V, as a function of position:

$$V = -2\pi q_b \left(\frac{y - L_1 - L_2}{S_c} \right)$$

$$+ q_c \left\{ \ln[4 \sinh^2(\pi(y-L_1)/S_c) + 4 \sin^2(\pi x/S_c)] - 2\pi L_2/S_c \right\}$$

$$+ q_a \left\{ \ln[4 \sinh^2(\pi y/S_a) + 4 \sin^2(\pi x/S_a)] - 2\pi(L_1+L_2)/S_a \right\}$$

$$+ \text{Constant} \quad . \quad (7)$$

Evaluating Eq. (7) at the surface of the electrodes with the appropriate potentials V_a, and V_c, the anode and cathode potentials, gives rise to two equations in the unknowns, q_a, q_b and q_c. The third equation is provided by the subsidiary condition that the field outside the chamber be constrained to zero.

Upon solving this system of equations for Q, these values may be substituted into Eq. (7) and the potential as a function of electrode voltages may be calculated. Figure 5 shows a plot of the potential as a function of y for the specific geometry of our detector at two x-values, x = 0 and x = 0.0635 cm with V_a = 1.0 and V_c = 0.4. At these voltages, the drift fields on either side of the cathode are uniform. Also, no charge is collected by the cathode although there is a low field region near the cathode wires associated with a saddle point on the potential surface.

The capacitance matrix may be derived from the system of equations described above. The elements of the capacitance matrix relate the effect on the charge of any electrode caused by changing the voltage of any other electrode. Thus for the specific geometry under consideration, the cathode capacitance, with the anode and pressure vessel grounded, is 198 pF. This value agrees to within 10% of the measured value. Cathode capacitance is an important parameter in chamber design, as will be shown below. The optimum position-signal processing parameters are intimately connected to cathode capacitance in terms of count rate and electronic position resolution. By comparison, the capacitance of a parallel plate capacitor of similar dimensions is 275 pF. The discrepancy is due to the work needed to move the charge from a uniform distribution on the plate to the circular geometry of the wires. However, provided that the ratio of interwire spacing to wire diameter is less than 100, the parallel plate approximation may be used in most practical cases.

The cathode signal is induced by positive ions falling through the strong 1/r electric field surrounding the anode wires. Thus, the signal is induced over several wires, and the span of the induced signal is of the order of the interelectrode gap. Since the cathode in this case is not a solid plane, but rather a linear array of wires, one must ask how much charge is induced on the cathode wires and how much is induced uselessly on the pressure vessel wall. That which is induced on the wall is not included in the measurement of the position of an event and hence position resolution suffers. An exact calculation of this quantity presents formidable mathematical difficulties. We are interested in the field induced by a point charge near the anode wire in the given chamber geometry; such a geometry has few symmetry properties. We can, however, calculate the charge induced on the cathode vs. the pressure vessel by an increment of charge spread uniformly over the anode. This figure, η, is a reasonable estimate of the performance of the actual detector with regard to induced charge. Therefore, η may be written as,

$$\eta = \frac{\Delta q_b}{\Delta q_a} = \frac{\Delta q_b/\Delta V_a}{\Delta q_c/\Delta V_a}$$

$$= \frac{C_{ba}}{C_{ca}} \qquad (9)$$

where C_{ba} is the box anode capacitance and C_{ca} is the cathode anode capacitance. η for our detector is equal to 0.09; negligible charge is lost to pressure vessel walls. We have measured this quantity experimentally with neutron induced pulses and found it to be in good agreement. This measurement is taken by comparing the anode signal to the sum of the two cathode signals, $1-\eta$ being the ratio of these two quantities.

5. Position Readout

5.1 Signal Processing

The charge division method determines the position of the event by calculating the ratio of the charge collected at one end of the resistive wire to the total collected charge. The charge division method of position readout has an important attribute, which it shares with several other readout methods. The position that the readout computes is the center of gravity of the currents induced on the cathode wires. Hence we have the capability of interpolating positions of events that occur between the cathode wires. Since the charge is always multiplied very close to the anode wires, the dimension at right angles to the direction of the anode wires has a spatial quantization. The other dimension exhibits a smooth variation in readout position vs. event position due to the interpolating nature of the readout.

Figure 6 shows a block diagram of the electronics used to read the position of a neutron capture event. Each end of the cathode is connected to a separate charge sensitive preamplifier. This general circuit has been described previously.[26] We have modified it in one important aspect, however. The input impedance of this circuit is shown to be[27]

$$R_{in} = \frac{1}{g_m}\,\frac{C_o}{C_f}$$

where C_o/g_m is the time constant of the dominant pole in the open loop gain of the preamplifier and C_f the feedback capacity. This expression is accurate so long as the signal time, τ, is less than C_o/g_m. Since $R_1 + R_2$ for each cathode is ~ 3000 ohms, it is important to keep the input resistance of the preamplifier small, otherwise the position sensitivity of the readout is reduced. To accomplish this end, the feedback capacity C_f was chosen to be 50 pF and the feedback resistor to be 1 megohm. These values gives the desired 50 μsec decay time. Under these conditions, the input resistance is measured to be approximately 50 ohms. The current waveform from the cathode is proportional to $(1+t/t_o)^{-1}$ when t_o is a parameter dependent on applied voltage, positive ion mobility, and chamber geometry.[28] Thus the voltage output of the preamplifier is proportional to $\ln(1+t/t_o)$, the integral of the current, i.e., charge. These are waveforms arising from ionization tracks in the gas of zero path length. For ionization paths of finite extent (the case for protons and triton in the reaction $He^3(n,p)H^3$), the waveforms will be further smeared out in time. The lower limit of the preamplifier bandwidth further alters the waveforms, making them decay with a time constant of approximately 50 μsec. Hence, rather than specify t_o, the risetime of the preamplifier output pulse is used to characterize the waveforms. For our configuration, the risetime (10% to 90% of the preamp output waveform) is measured to be 0.5 μsec

Unfortunately, the current output from each cathode is sufficiently small that the noise from various dissipative components in the electronics can cause apparent spatial resolution effects comparable to those caused by the finite path length of the products in the neutron capture reaction. Of these sources, the dominant noise component is generated by the readout wire itself. Thus, the optimization of circuit parameters against these noise effects is necessary. An extensive analysis of this subject has been presented in Ref. (27), from

which we will quote results.

The output of the charge-sensitive preamplifiers is further shaped and amplified by two delay line clipped amplifiers. These have shaping of 1 μsec delay lines followed by RC integration with a time constant of .25 μsec. This shaping enables the position determination to be made based on virtually all the charge from an event induced on the cathodes. Although position linearity does not suffer if all the charge is not collected, position resolution does. On the other hand, if the measurement time is extended too long, the position resolution will also worsen due to noise as described below. Hence, there is an optimum shaping for minimum position resolution.

For the shaping we have chosen, we may calculate the position resolution expected on the basis of electronic noise alone. We wish this noise contribution to resolution to be significantly less than that caused by the charged particle path lengths from the He^3 reaction. First, define R_D and C_D as the total resistance and capacity of the cathode, τ_F as the width of the delay line amplifier shaping function as its base, assuming it to be trapezoidal in shape with the top of the trapezoid being 0.6 of the base. Now, the equivalent noise charge input into the cathode can be written,

$$\overline{ENC_p^2} = 1.47\ kT\ \frac{\tau_F}{R_D} \quad \text{(rms)} \qquad (10)$$

and the relative electronic resolution of the cathode is

$$\frac{\Delta\ell}{\ell} = 2.35\ \frac{ENC_p}{Q_s} \quad \text{(FWHM)} \qquad (11)$$

where kT is Boltzman's constant multiplied by temperature. Thus in our case $R_D = 3000\ \Omega$, $C_D = 200$ pF, $\tau_F = 1.1$ μsec, $ENC_p = 9.29 \times 10^3$ rms electrons and $\frac{\Delta\ell}{\ell} = 2.18 \times 10^4/Q_s$ where Q_s is the charge collected by the cathode. We expect to collect 5×10^6 electronic charges on each cathode. Therefore, $\frac{\Delta\ell}{\ell} = 0.437\%$. Using a lumped RC line with appropriately distributed resistance and capacitance, we have measured $\frac{\Delta\ell}{\ell} = 0.472$, confirming the calculation. This position resolution is equivalent to approximately 1 mm in spatial resolution over 17 cm. Since the particle range is expected to yield a resolution function of ~ 3 mm, the initial criterion for the readout is satisfied. Figure 7 shows a plot of system position output vs. injected charge position on an RC line with linearly distributed resistances. This RC line simulates the parameters measured in the detector. The non-linearity of this graph is less than 0.3% as determined by fitting the data to a quadratic function, where non-linearity is defined as one half the ratio of the quadratic term to the total measured position at the maximum abcissa. In the next section, we shall show similar results taken from actual neutron data.

The above analysis defines the basic performance of the system. The remainder of the circuitry shown in the block diagram (Fig. 6) serves basically to realize the division function. The unipolar outputs of the linear amplifiers are added in one channel to give the total charge collected from the cathode. This sum signal and the unnormalized position signal are applied to the linear inputs of a pair of linear gates and stretchers. These linear gates are strobed by a signal derived from the sum of the bipolar outputs of the delay line clipped amplifiers. This sum is processed through a timing single channel analyzer that provides energy discrimination against noise and possible gamma ray contamination of the charged particle energy spectrum. It is this output which strobes both the linear gates and the divider, the output of which is the measured position signal.

Each cathode has electronics identical to that described above. In addition, a time coincidence is required between the timing single channel outputs of each cathode to accept a valid event. The analogue output signals are converted in separate analogue-to-digital converters and the digital result is stored in 12,000 memory locations of medium size digital computer. For further analysis, the results are transferred to magnetic tape and processed off-line.

5.2 Analogue Divider Circuitry

The complete circuit diagram of the analogue divider is shown in Figs. 8 and 9. The divider is based on logarithmic conversion of the two input variables, and on the exponential conversion of the difference of the two logarithms. The logarithmic-exponential conversions are performed using the exponential characteristics of semiconductor junctions. This solution was chosen because of inherently good accuracy over a large dynamic range, and since the development of a fast logarithmic converter circuit[29] made fast conversion possible. It can be shown that the temperature dependence of such a divider circuit can be reduced to a term $(Y/X)^{AT_\ell/T_e}$, where T_ℓ and T_e are absolute temperatures of the junctions used for logarithmic and exponential conversion, and A is the gain of the difference amplifier. To maintain nearly the same temperature for the two logarithmic converters and for the exponential converter an integrated monolithic multiple transistor circuit was used, and the maximum power dissipation was kept at a few milliwatts. Fast logarithmic conversion was discussed in detail in Ref. 29. Inputs to logarithmic converters are dc coupled. A small adjustable correction is provided for the residual emitter resistance in both the logarithmic and exponential circuits. In the former, a linear term (a constant fraction of the input) is subtracted from the logarithmic output. In the exponential circuit, a linear term (constant fraction of the output) is added to the drive via the emitter.

The exponential converter is ac coupled at the input, and it incorporates a baseline restorer (transistors 14 to 22). This solution was chosen to achieve dc stability. This exponential converter was developed from a circuit by Goulding.[30] The gain A for the difference of logarithms should be unity. (Otherwise the output is an exponential function of the ratio.) The output of the divider is strobed during the flat top portion of the input signals, to avoid large signals when the denominator is small or zero.

The circuit can be adjusted to an accuracy of the ratio of 0.2% over a dynamic range of 20 to 1. The division is performed in 500 nsec.

6. Results

The chamber, as described in the previous sections, has been tested for a variety of parameters that indicate its performance under real experimental conditions. Among these parameters are spatial resolution, spatial non-linearity, spatial non-uniformity in efficiency, wall effect, background gamma-ray sensitivity, detection efficiency, event resolving time and event processing time. A summary of this information along with the physical chamber characteristics is presented in Table II.

Figure 10 shows the pulse height spectrum derived

from pulses summed from the two ends of the cathode, as shown in the electronic block diagram (Fig. 6). The other cathode produces the same spectrum. The pulse height in this spectrum is proportional to the total charge collected by the anode and, hence, to the total energy deposited in the detector by the reaction products from $He^3(n,p)H^3$, (Q = 764 keV).

The energy resolution displayed in the energy spectrum (Fig. 10) is worse than one usually sees in single wire He^3 filled neutron detectors. At lower voltages, and hence lower gains, the spectrum shape is comparable to that obtained in Refs. (6-9) and the energy resolution is similar. However, as the gain of the chamber is increased, the spectrum shape deteriorates to that shown in Fig. 10. It is reasonable to ascribe the degrading of the energy spectrum to space charge effects.[31] Different track orientations of the reaction products yield different apparent charge gains due to charge density effects around the anode wire. The choice of operating point and gain was made on the basis of spatial resolution desired vs. tolerable gamma-ray background. At high gains the energy resolution of the neutron peak deteriorates. Therefore, to remain at the same neutron efficiency one must accept more gamma background. All tests reported in this section were performed with discriminators set at 370 keV, Fig. (10).

It is difficult to define gamma-ray sensitivity in the typical reactor environment since many gamma-rays of different energy are produced. However, in the environment in which this detector operated, (BNL HFBR) the gamma-ray background is 5 counts/sec with the primary beam on and stopped on boron-poly. A more systematic definition of gamma-ray sensitivity was made by placing a 1 mCi Co^{60} source 60 cm from the face of the detector, oriented at normal incidence. With the threshold at 370 keV, the gamma sensitivity is 2.7×10^{-6} gammas detected/incident gamma.

The neutron detection efficiency of the chamber has been measured by intercepting the incident neutron beam (λ = 2.8 Å) with a 95% efficient BF_3 detector. The ratio of the event rate in the different detectors gives the detection efficiency of the He^3 position-sensitive detector. We measure this number to be 70%. Calculation (Fig. 3) yields an efficiency of 82% for this wavelength. The major part of the discrepancy between these values is most likely due to wall effect. This effect is evident in Fig. 10 in the slight bump to the left of the main peak, a feature caused by the non-uniform energy loss of those tritons that strike the chamber wall. The energy of this bump equals the total Q-value minus the triton energy (573 keV). The proton wall effect is partially obscured by the rising gamma background. Otherwise, a similar feature would occur at 191 keV.[21]

We now describe the measurement of spatial resolution vs. charge collected at the detector anode. The electronic contribution to the spatial resolution may be separated from the physical contribution by varying the detector anode voltages. We have performed this measurement and results are shown in Fig. 11. The abcissa is the voltage between cathode and anode, which determines charge gain. The ordinate is the FWHM spatial resolution of the detector parallel to the anode wires. Above 2800 volts the spatial resolution saturates due to physical chamber parameters at 2.5 ± 0.1 mm. The higher voltages lead to problems with background rejection as described above. Hence, the detector is operated at approximately 2800 volts and a spatial resolution of 3.1 ± 0.1 mm.

The contribution to the spatial resolution from the physical path length of the reaction products is 2.5 ± 0.1 mm. In Section 3, we have calculated the physical range to be 2.76 mm using tabulated range and energy loss data. This agreement is quite close considering the difficulties in calculating specific ionization at low values of proton and triton energy.

We have measured two quantities affecting count rate capacity of this detector, namely event resolving time and event processing time. The former may be defined as the time in which the detector is sensitive to event pileup. Such pileup can lead to false position calculations. The latter refers to the time in which the system is insensitive to incoming data. Events occurring in this time period are lost; however, the validity of the event being analyzed is not compromised. The measured values are, at present, 1 μsec for event resolving time and 3 μsec for event processing time. We are operating in a conservative manner at present, and a factor of two reduction in these times is wholly feasible.

Figure 12 shows a sweep of the primary neutron beam across the detector in a direction parallel to the anode wires. Data were taken every 1.46 cm across the detector face at the midline of the detector. Also shown on the same figure is true position of the beam vs. measured position. There is a residual nonlinearity in the measurement of true position vs. measured position. This error is approximately 1% of full scale or 0.17 cm and may easily be described by a simple quadratic function.

The detection efficiency is uniform to within 3% across the entrance window of the detector. Any effect here is caused by gain variations across the detector, which in effect change the pulse height threshold setting as a function of position. We have observed this effect by gating a multichannel analyzer on spatially distinct areas of the detector. Regions of increased gain correspond to regions of increased efficiency.

Figure 13 is a contour plot of a complete two-dimensional detector scan with the primary neutron beam. A well collimated neutron beam was swept across the detector in a regular rectilinear pattern. Each contour represents approximately 20% of the full peak height. The increment along the x-axis is 1.46 cm and along the y-axis 2.54 cm. Each line in y, upon integrating over the peak in the y direction, yields a plot similar to that shown in Fig. 11. From this figure we may deduce that there is no interaction between coordinates in position determination which would possibly give rise to "barrel" or "pincushion" distortion. Thus, the two axes are completely independent. This fact facilitates any correction needed for the residual non-linearity left in the read-out system. Each axis may thus be corrected independently from the other.

Figure 14 shows scattering data (intensity vs. angle 2θ) from retinal rods, the light transducing system of the eye. Delicate samples such as these are easily damaged by radiation and ambient conditions. The maximum neutron exposure time for these samples in oxygenated Ringer solution is about eight hours. Conventional single counter systems, which scan in angle 2θ point by point, do not have the sensitivity to adequately measure the neutron diffraction pattern from such samples. The bottom three traces show the accumulated intensity profile of ten frog retinas scanned by a conventional system.[1] The second and third traces represent data collected in the same fashion as the bottom one, but using an improved surgical and sample mounting technique. The top trace represents data collected from two retinas with the two-dimensional detector,

using the improved mounting technique and a smaller sample. This data extends to larger angles, permitting analysis of the membrane structures to the desired resolution.[32] The use of a much smaller sample results in better data with considerably less effort.

Acknowledgements

We wish to acknowledge the assistance of R. Dillingham and J. Gatz in the fabrication of this detector. C. Nawrocki and J. Trebing aided in its assembly, and E. Caruso helped with testing and checkout. B. Gaer aided in the preparation of this manuscript.

Table I

Neutron-Charged Particle Reactions Suitable for Thermal Neutron Detection[5]

	Reaction	Q-Value	Thermal Cross Section
a)	$B^{10} + n \longrightarrow Li^{7} + \alpha$	+2.79MeV (6.1%)	
	$\searrow Li^{7*} + \alpha$	+2.31MeV (93.9%)	3840 ± 11b
	$\searrow Li^{7} + \gamma$	+0.478 MeV	
b)	$Li^{6} + n \rightarrow H^{3} + \alpha$	+4.786 MeV	936 ± 6b
c)	$He^{3} + n \rightarrow H^{3} + p$	+0.764 MeV	5327 ± 10b

Table II

Characteristics of Two-Dimensional Position-Sensitive Detector

1. Neutron detection efficiency at 2.8 Å wavelength..... 70%
2. Position resolution at $V_a - V_c$ = 2800 volts..... 3.1mm
3. Positional uniformity of detection efficiency... 3%
4. Integral linearity..... 1%
5. Differential linearity..... 0.1%/% of full scale
6. Event resolving time..... 1 μsec
7. Event processing time..... 3 μsec
8. Gamma-ray sensitivity (Co^{60}): 2.7×10^{-6} γ-detected/incident-γ
9. Sensitive area..... 18cm x 18cm
10. Gas filling composition (absolute pressure)..... 6 atmos. He^3 / 4 atmos. A / 0.5 atmos. CO_2

References

1. B. P. Schoenborn and A. Nunes, Annual Review of Biophysics and Bioengineering, 1, 529(1972).
2. B. Rossi and H. Staub, Ionization Chambers and Counters, McGraw-Hill, New York (1949).
3. D. H. Wilkinson, Ionization Chambers and Counters, Cambridge Univ. Press, Cambridge (1950).
4. S. A. Korff, Electron and Nuclear Counters, Van Nostrand, New York (1946).
5. K. H. Beckurts and K. Wirtz, Neutron Physics, Springer-Verlag, Berlin (1964).
6. R. Batchelor, R. Aves, and T. H. R. Skyrme, Rev. Sci. Instr., 26, 1037 (1955).
7. A. R. Sayres, K. W. Jones, and C. S. Wu, Phys. Rev., 122, 1853(1961).
8. W. R. Mills, et al., Rev. Sci. Instr., 33, 866(1962).
9. V. E. Krohn, Jr., Rev. Sci. Instr., 35, 853(1964).
10. R. Grove, I. Ko, B. Keskovar and V. Perez-Mendez, Nucl. Instr. & Meth. 99, 381(1970).
11. D. M. Lee, S. E. Sobottka and H. A. Thiessen, Nucl. Instr. & Meth. 104, 179(1972).
12. J. R. Gilland and J. G. Eaming, Nucl. Instr. & Meth. 104, 241(1972).
13. K. Louterjung, et al., Nucl. Instr. & Meth. 22, 117(1963).
14. W. R. Kuhlmann, et al., Nucl. Instr. & Meth. 40, 118(1966).
15. G. Kalbitzer and W. Melzer, Nucl. Instr. & Meth. 56, 301(1967).
16. R. B. Owen and M. L. Awcock, IEEE Trans. Nucl. Sci. NS-15, 290(1968).
17. C. J. Borkowski and M. K. Kopp, Rev. Sci. Instr. 39, 1515(1968).
18. C. J. Borkowski and M. K. Kopp, IEEE Trans. Nucl. Sci. NS-17, 340(1970).
19. C. J. Borkowski and M. K. Kopp, IEEE Trans. Nucl. Sci., NS-19, 161(1972).
20. Haim Zaklad, UCRL-20690 (1971).
21. S. Shalev, Z. Fishelson and J. M. Cuttler, Nucl. Instr. & Meth. 71, 292(1969).
22. L. C. Northcliffe and R. F. Schilling, Nucl. Data, 7, 233(1970).
23. R. D. Evans, The Atomic Nucleus, McGraw-Hill, New York(1955).

24. G. Charpak, Ann. Rev. Nucl. Sci., 20, 195(1970).

25. K. Spangenberg, Vacuum Tubes, McGraw-Hill, New York (1948).

26. V. Radeka, Proc. Intern. Symp. Nucl. Electronics, 1, 46-1, *Versailles* (1968).

27. V. Radeka, IEEE Trans. Nucl. Sci., NS-21, 51(1974).

28. G. R. Richer, Jr. and J. J. Gomez, Rev. Sci. Instr. 49, 227(1969).

29. V. Radeka, Nucl. Instr. & Meth. 113, 401(1973).

30. F. S. Goulding, D. A. Landis, J. Cerny, III, and R. H. Pehl, IEEE Trans. Nucl. Sci., NS-11, 388(1964).

31. G. C. Hanna, et al., Phys. Rev. 75, 985(1949).

32. M. Reager, et al., J. Med. Biol. (in press).

FIGURE CAPTIONS

Fig. 1 a) Schematic diagram of multiwire proportional chamber geometry.

b) Schematic diagram showing parameters for the electric field calculation.

Fig. 2. Calculated detector efficiency vs. neutron wavelength for a gas filling of 40% argon and 60% He^3 by volume at 10 atmospheres.

Fig. 3. Detection efficiency of 4 Å neutrons vs. gas composition at 10 atmospheres pressure (curve A) and proton range vs. gas composition at 10 atmospheres pressure for two gases, argon and krypton, (curves B and C).

Fig. 4. One-dimensional spatial resolution function, D(p), under two conditions: A, uniform ionization to a cutoff range R_p, the proton range and B, specific ionization derived from Bragg ionization curves.

Fig. 5. Electric potential as a function of y for the specific geometry of our detector at two x-values, x = 0 and x = 0.0635 cm with $V_a = 1.0$ and $V_c = 0.4$.

Fig. 6. Block diagram of the electronics used to read the position of a neutron capture event. Labeled values are as follows: $R_a = 100$ MΩ, $C_a = 0.015$ μF, $C_i = 0.01$ μF, $C_f = 50$ pF, $R_f = 1$ MΩ, V_c and V_a are cathode and anode voltages.

Fig. 7. Position output vs. injected charge position on an RC line with linearly distributed resistances.

Fig. 8. Fast analog divider based on logarithmic-exponential conversion.

Fig. 9. Auxilliary circuits for the analog divider in Fig. 8 (linear gate, output stage and strobe control).

FIGURE CAPTIONS (Cont'd.)

Fig. 10. Pulse height spectrum derived from pulses summed from each of the two ends of the detector cathode.

Fig. 11. Measured position resolution (FWHM) vs. applied cathode to anode potential, $V_a - V_c$.

Fig. 12. Sweep of the primary neutron beam across the detector in a direction parallel to the anode wire. Data were taken every 1.46 cm across the detector face at the midline of the detector.

Fig. 13. Contour plot of a complete two-dimensional detector scan with the primary neutron beam.

Fig. 14. Scattering data (intensity vs. angle 2θ) from retinal rods, the light transducing system of the eye: the bottom three traces are taken with conventional techniques (see text). The top trace is taken using the position-sensitive neutron detector.

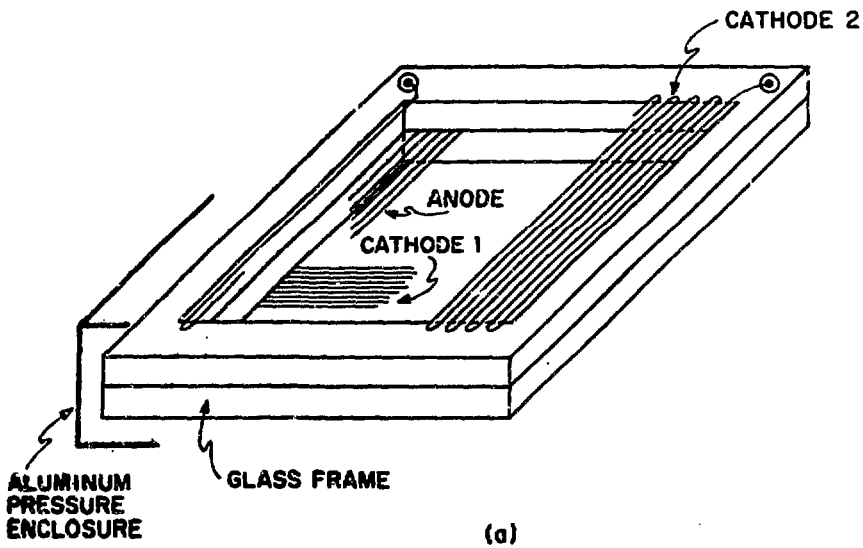
CATHODE 2
ANODE
CATHODE 1
ALUMINUM PRESSURE ENCLOSURE
GLASS FRAME

(a)

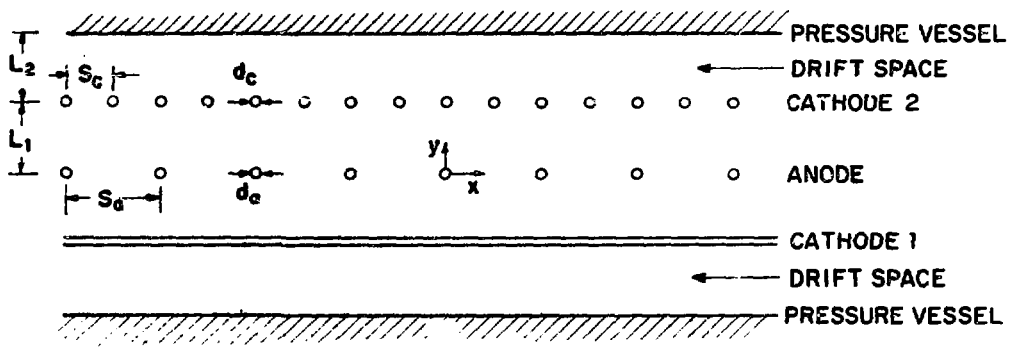
PRESSURE VESSEL
DRIFT SPACE
CATHODE 2
ANODE
CATHODE 1
DRIFT SPACE
PRESSURE VESSEL
L2
L1
Sc
dc
Sa
da
y
x

(b)

FIGURE 1

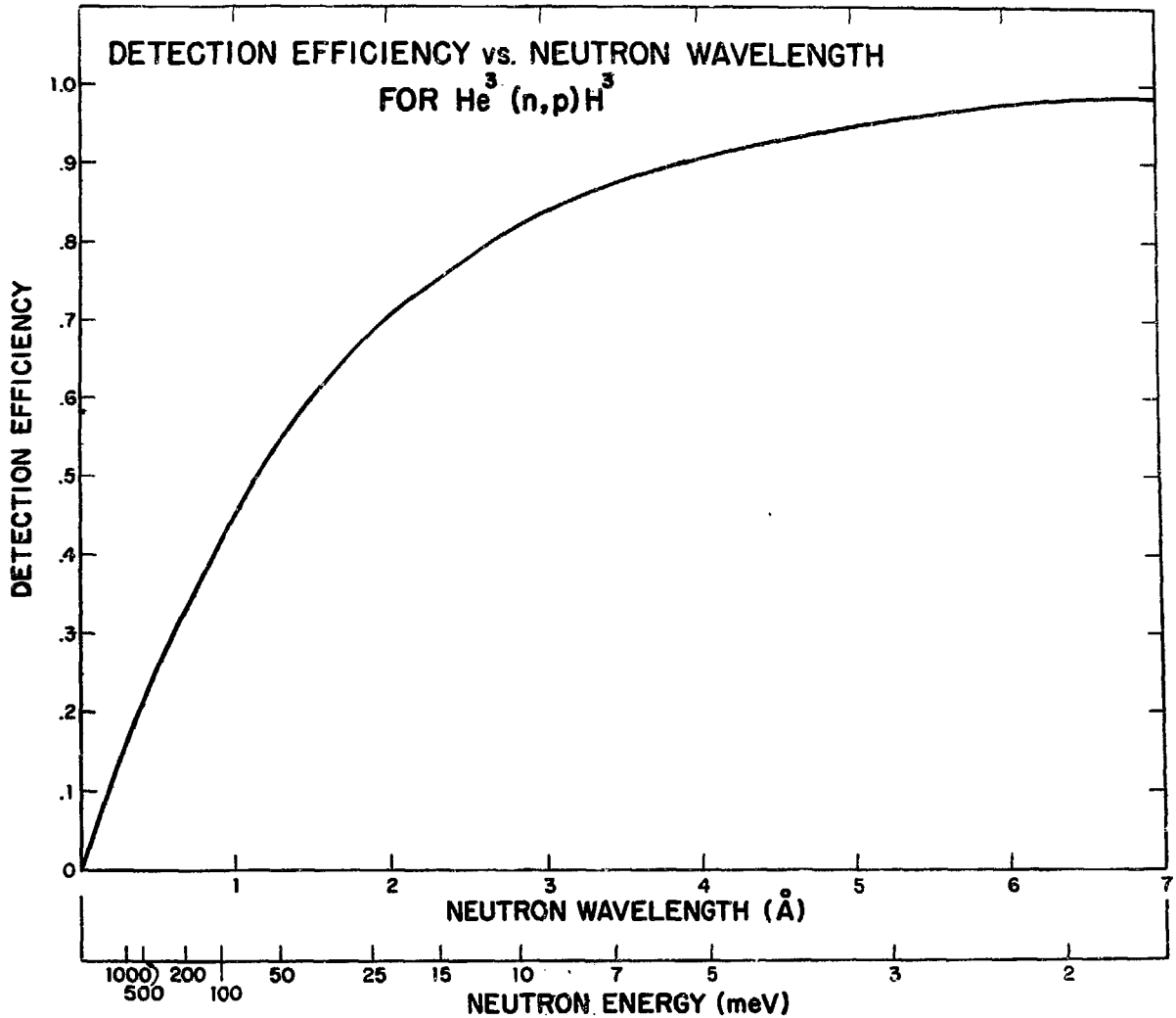
DETECTION EFFICIENCY vs. NEUTRON WAVELENGTH
FOR He3 (n,p) H3
DETECTION EFFICIENCY
1.0
.9
.8
.7
.6
.5
.4
.3
.2
.1
0
1
2
3
4
5
6
7
NEUTRON WAVELENGTH (Å)
1000
500
200
100
50
25
15
10
7
5
3
2
NEUTRON ENERGY (meV)

FIGURE 2

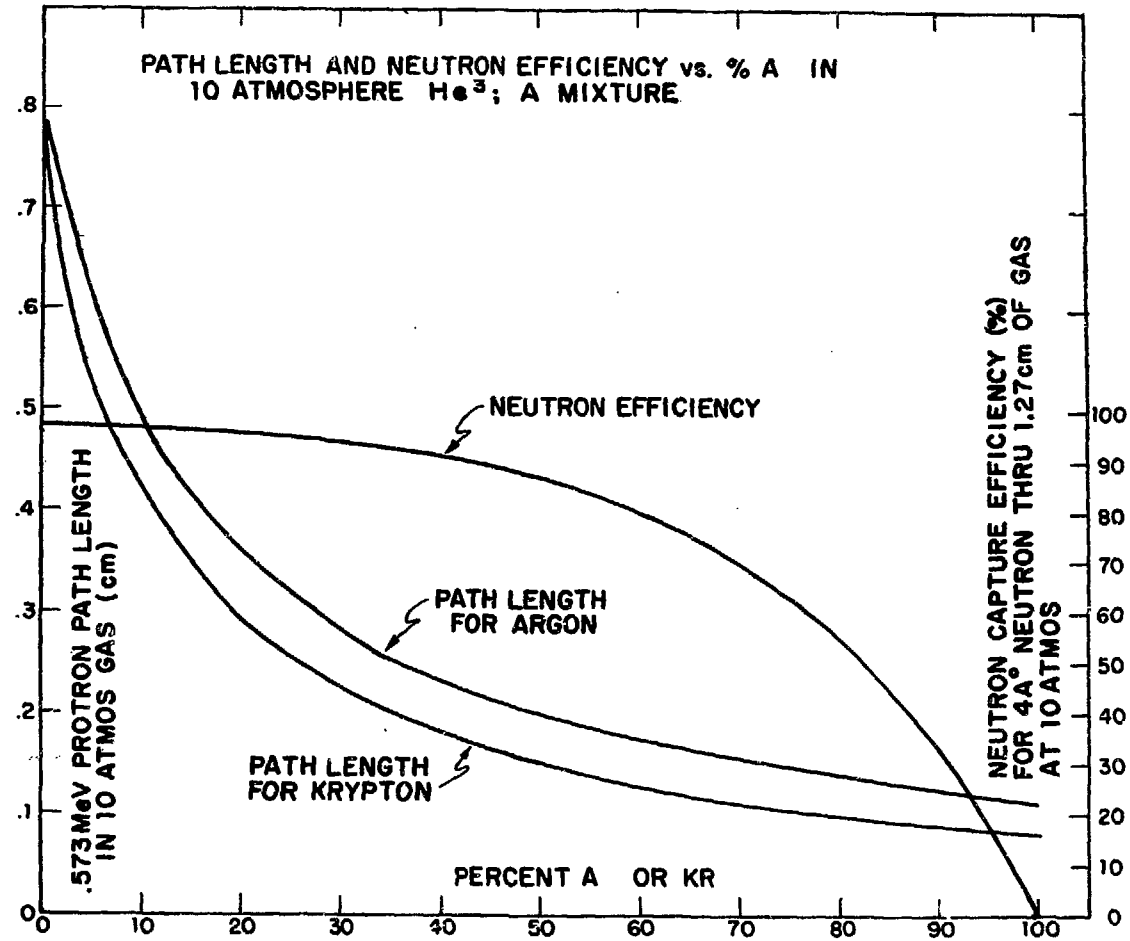
PATH LENGTH AND NEUTRON EFFICIENCY vs. % A IN
10 ATMOSPHERE He³; A MIXTURE
NEUTRON EFFICIENCY
PATH LENGTH
FOR ARGON
PATH LENGTH
FOR KRYPTON
.573MeV PROTRON PATH LENGTH
IN 10 ATMOS GAS (cm)
NEUTRON CAPTURE EFFICIENCY (%)
FOR 4A° NEUTRON THRU 1.27cm OF GAS
AT 10 ATMOS
PERCENT A OR KR
0
.1
.2
.3
.4
.5
.6
.7
.8
0
10
20
30
40
50
60
70
80
90
100

FIGURE 3

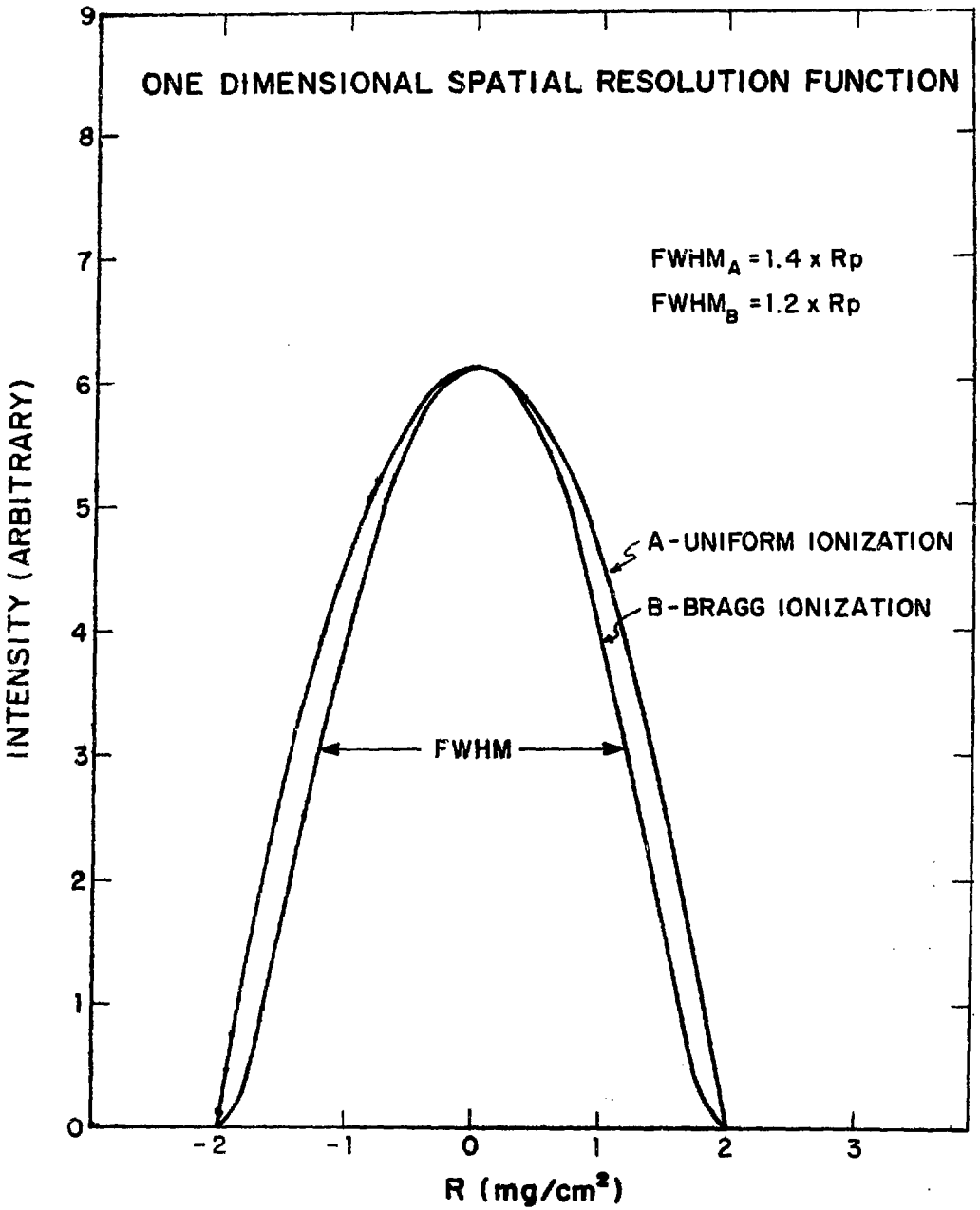
ONE DIMENSIONAL SPATIAL RESOLUTION FUNCTION
FWHM$_A$ = 1.4 x Rp
FWHM$_B$ = 1.2 x Rp
A - UNIFORM IONIZATION
B - BRAGG IONIZATION
FWHM
INTENSITY (ARBITRARY)
R (mg/cm^2)
0
1
2
3
4
5
6
7
8
9
-2
-1
0
1
2
3

FIGURE 4

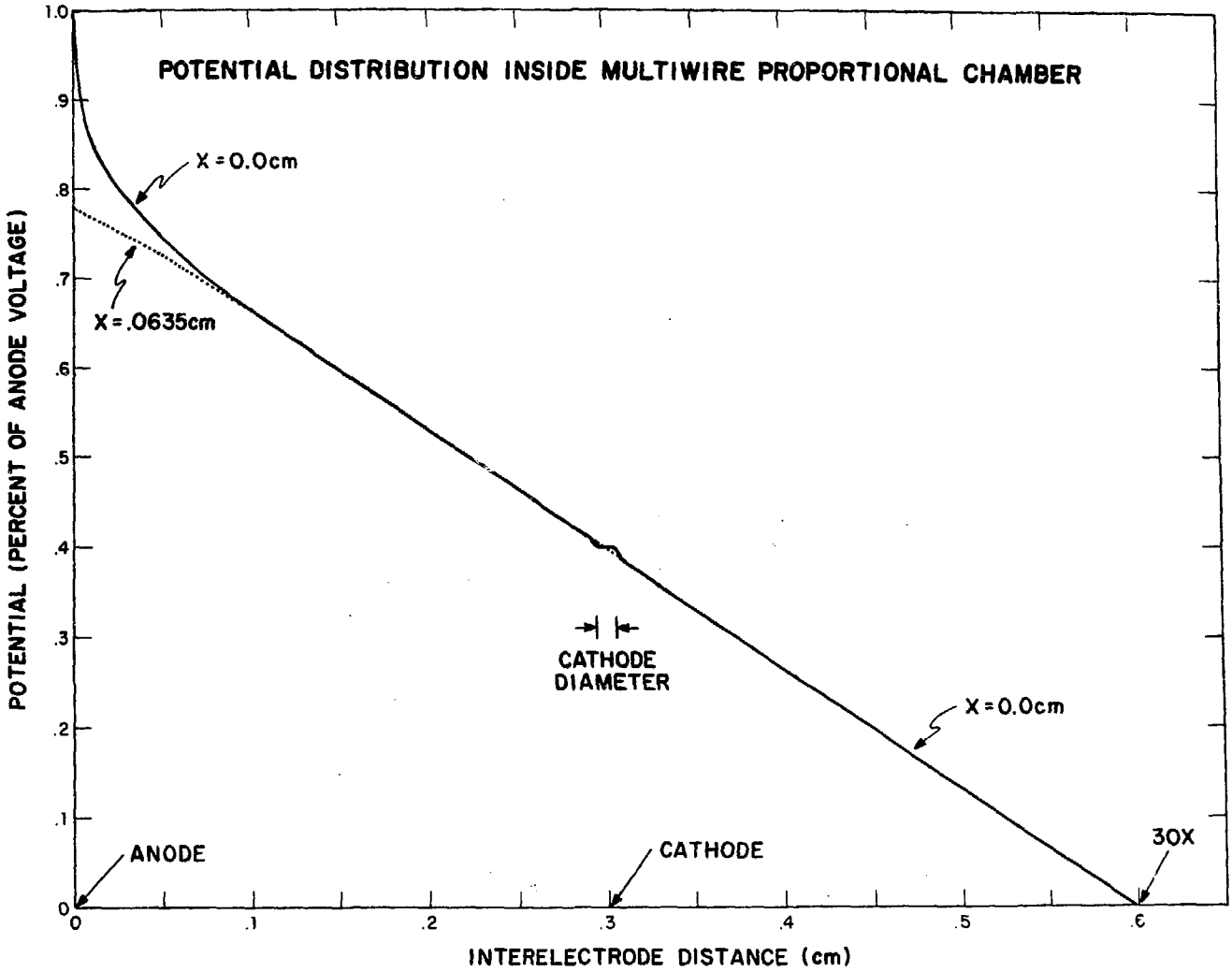
POTENTIAL DISTRIBUTION INSIDE MULTIWIRE PROPORTIONAL CHAMBER
POTENTIAL (PERCENT OF ANODE VOLTAGE)
INTERELECTRODE DISTANCE (cm)
X = 0.0cm
X = .0635cm
CATHODE DIAMETER
X = 0.0cm
ANODE
CATHODE
30X
1.0
.9
.8
.7
.6
.5
.4
.3
.2
.1
0
0
.1
.2
.3
.4
.5
.6

FIGURE 5

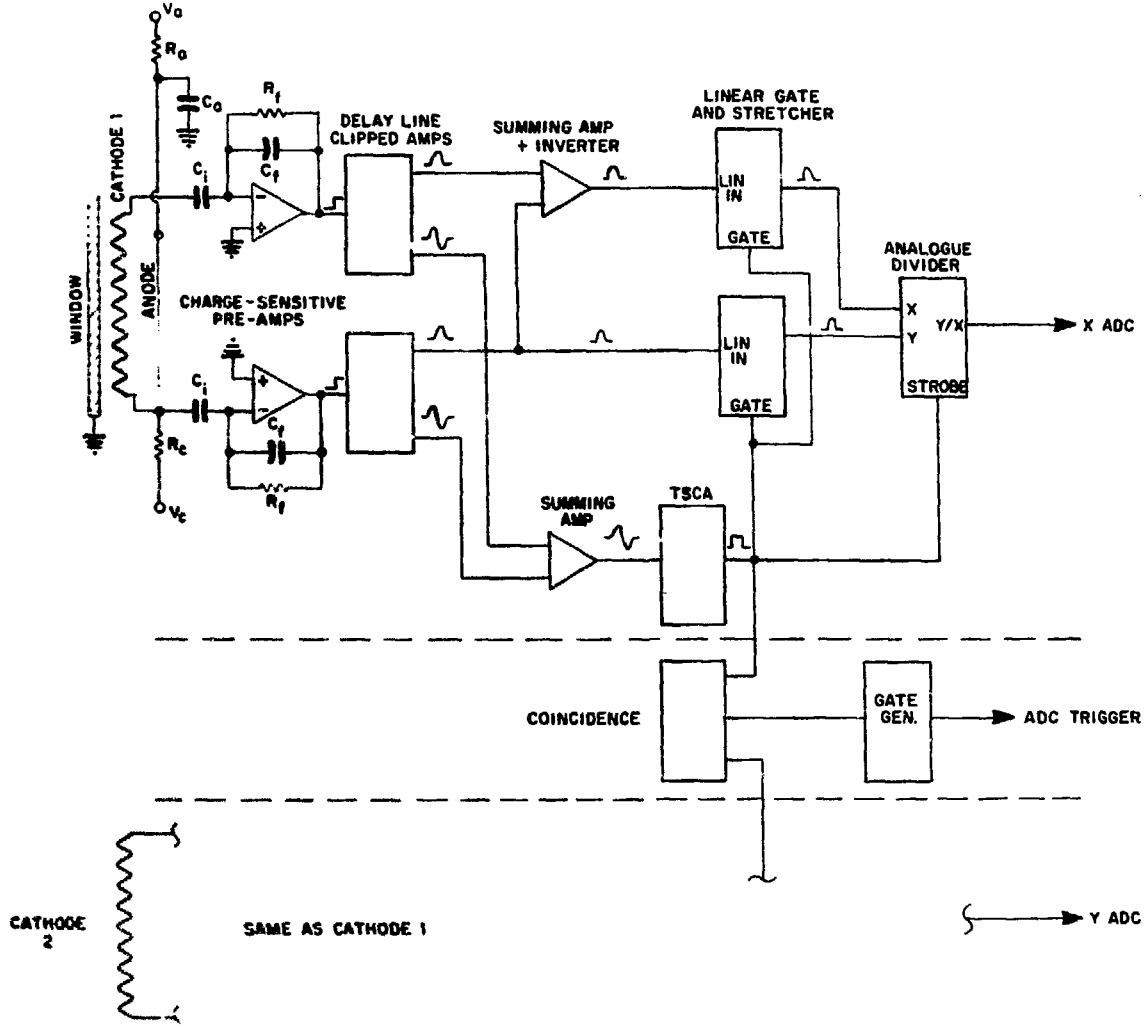
V_a
R_a
C_a
R_f
C_f
C_i
CATHODE 1
WINDOW
ANODE
DELAY LINE CLIPPED AMPS
SUMMING AMP + INVERTER
LINEAR GATE AND STRETCHER
LIN IN
GATE
ANALOGUE DIVIDER
X
Y
Y/X
STROBE
X ADC
CHARGE-SENSITIVE PRE-AMPS
R_c
V_c
SUMMING AMP
TSCA
COINCIDENCE
GATE GEN.
ADC TRIGGER
CATHODE 2
SAME AS CATHODE 1
Y ADC

FIGURE 6

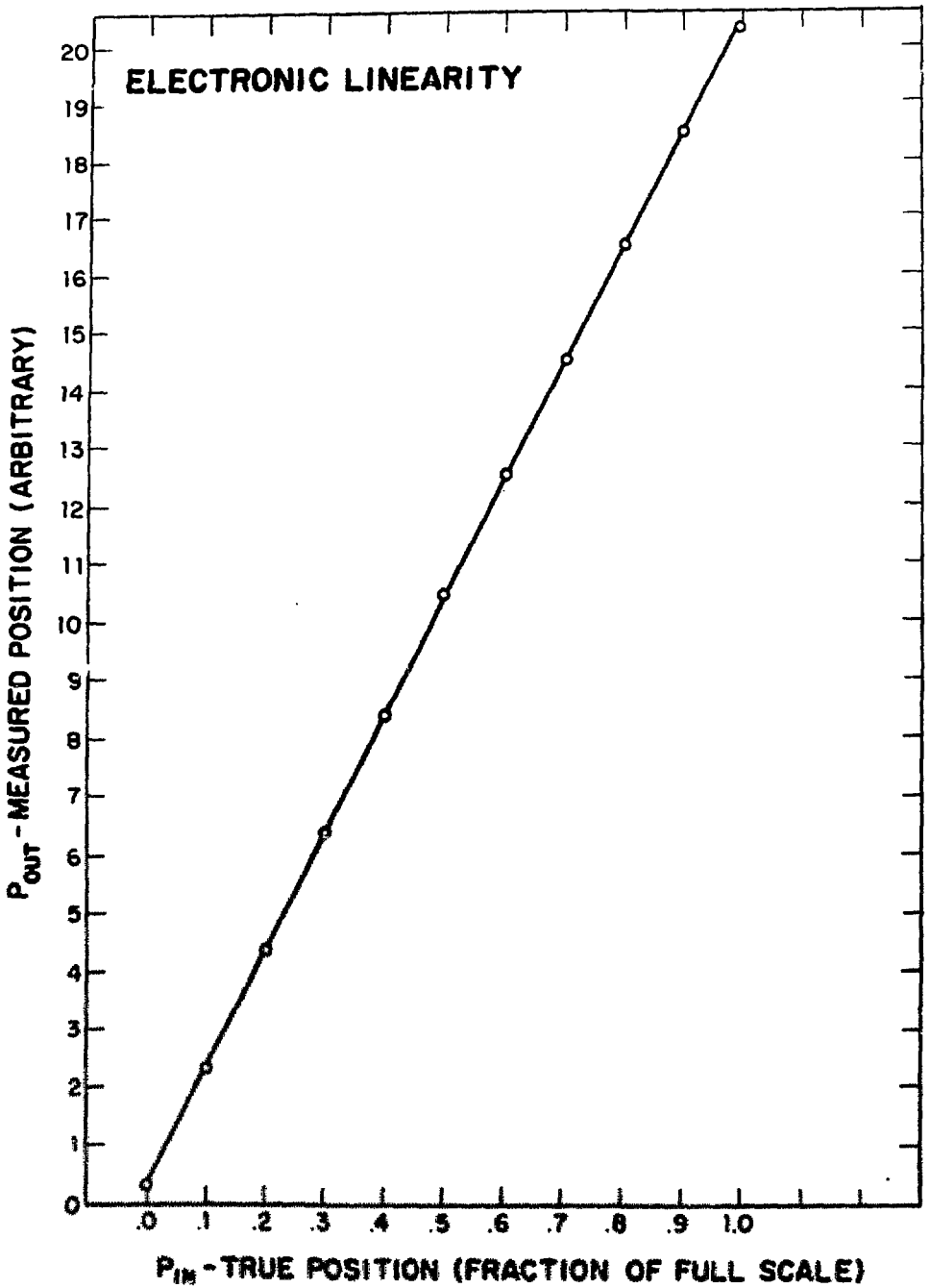
ELECTRONIC LINEARITY
P_{OUT} - MEASURED POSITION (ARBITRARY)
P_{IN} - TRUE POSITION (FRACTION OF FULL SCALE)
0
1
2
3
4
5
6
7
8
9
10
11
12
13
14
15
16
17
18
19
20
.0
.1
.2
.3
.4
.5
.6
.7
.8
.9
1.0

FIGURE 7

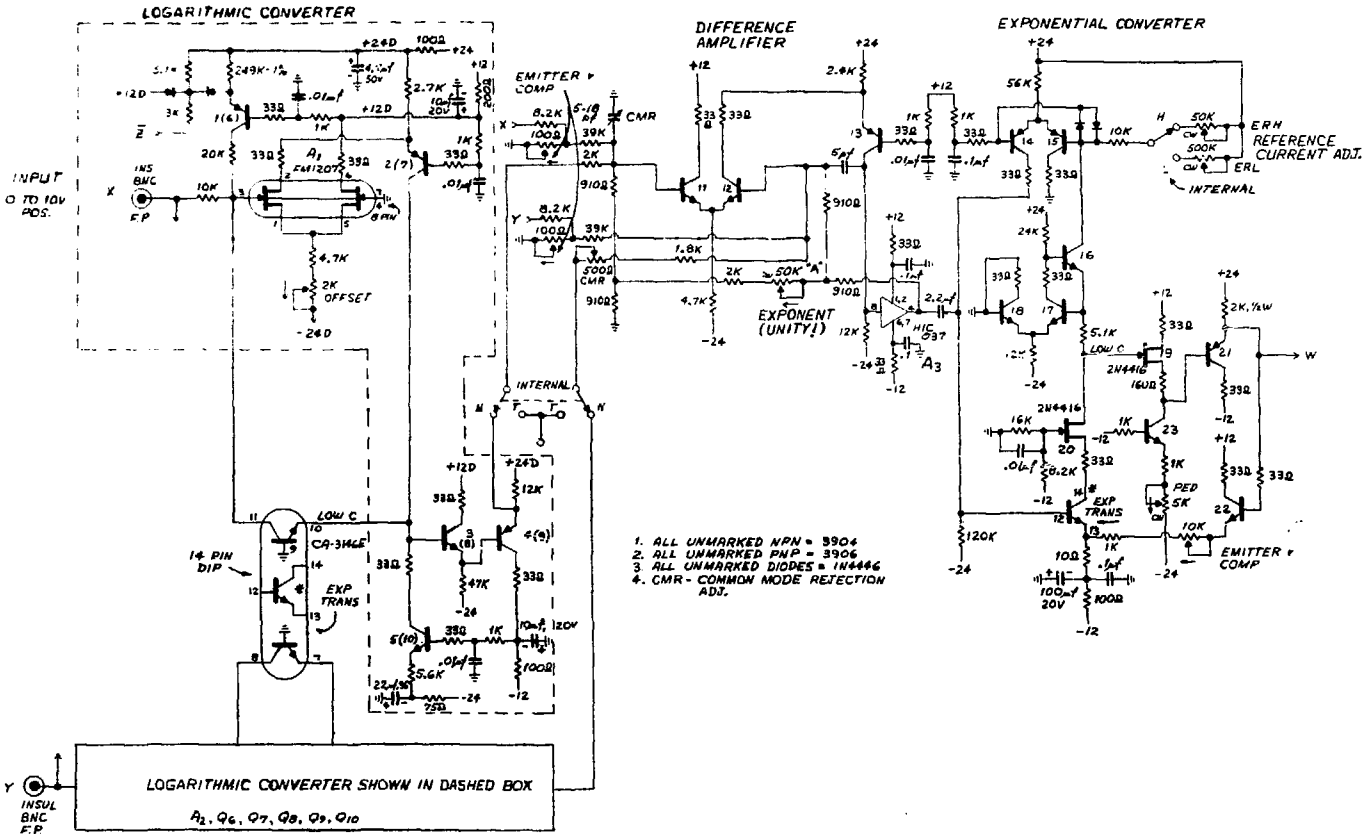
LOGARITHMIC CONVERTER
DIFFERENCE AMPLIFIER
EXPONENTIAL CONVERTER
INPUT
0 TO 10V
POS.
INS BNC F.P
EMITTER COMP
CMR
EXPONENT (UNITY)
INTERNAL
EXTERNAL
REFERENCE CURRENT ADJ.
ERN
ERL
2K OFFSET
LOW C
CA-3146E
14 PIN DIP
EXP TRANS
PED 5K
1. ALL UNMARKED NPN = 3904
2. ALL UNMARKED PNP = 3906
3. ALL UNMARKED DIODES = IN4446
4. CMR - COMMON MODE REJECTION ADJ.
LOGARITHMIC CONVERTER SHOWN IN DASHED BOX
A2, Q6, Q7, Q8, Q9, Q10
INSUL BNC F.P

FIGURE 8

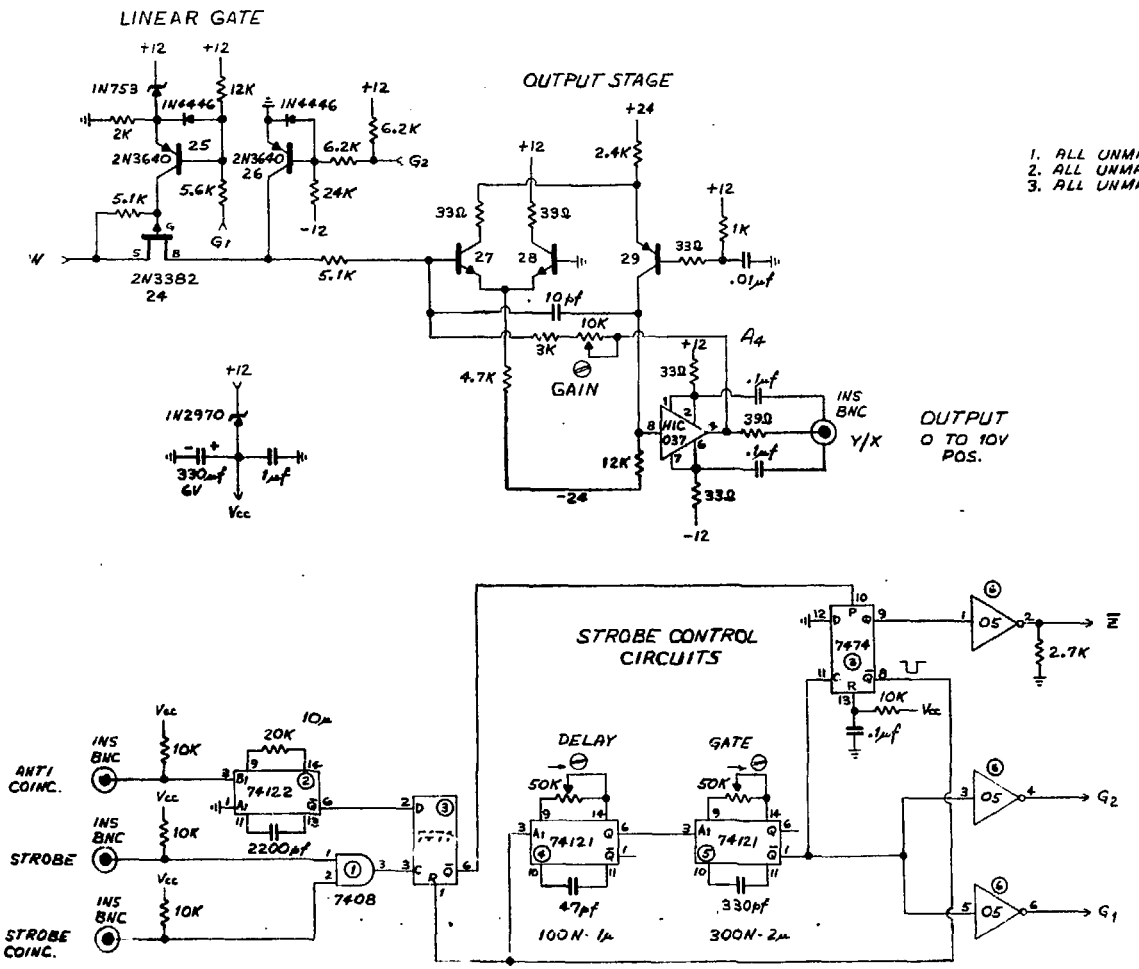
LINEAR GATE
OUTPUT STAGE
STROBE CONTROL CIRCUITS
1. ALL UNMARKED NPN = 3904
2. ALL UNMARKED PNP = 3906
3. ALL UNMARKED DIODES = IN4446
GAIN
INS BNC
Y/X
OUTPUT
0 TO 10V
POS.
ANTI COINC.
STROBE
STROBE COINC.
DELAY
GATE
7408
7474
74121
74122
7405
2N3640
2N3382
IN753
IN2970
MIC 037
100N- 1μ
300N- 2μ

FIGURE 9

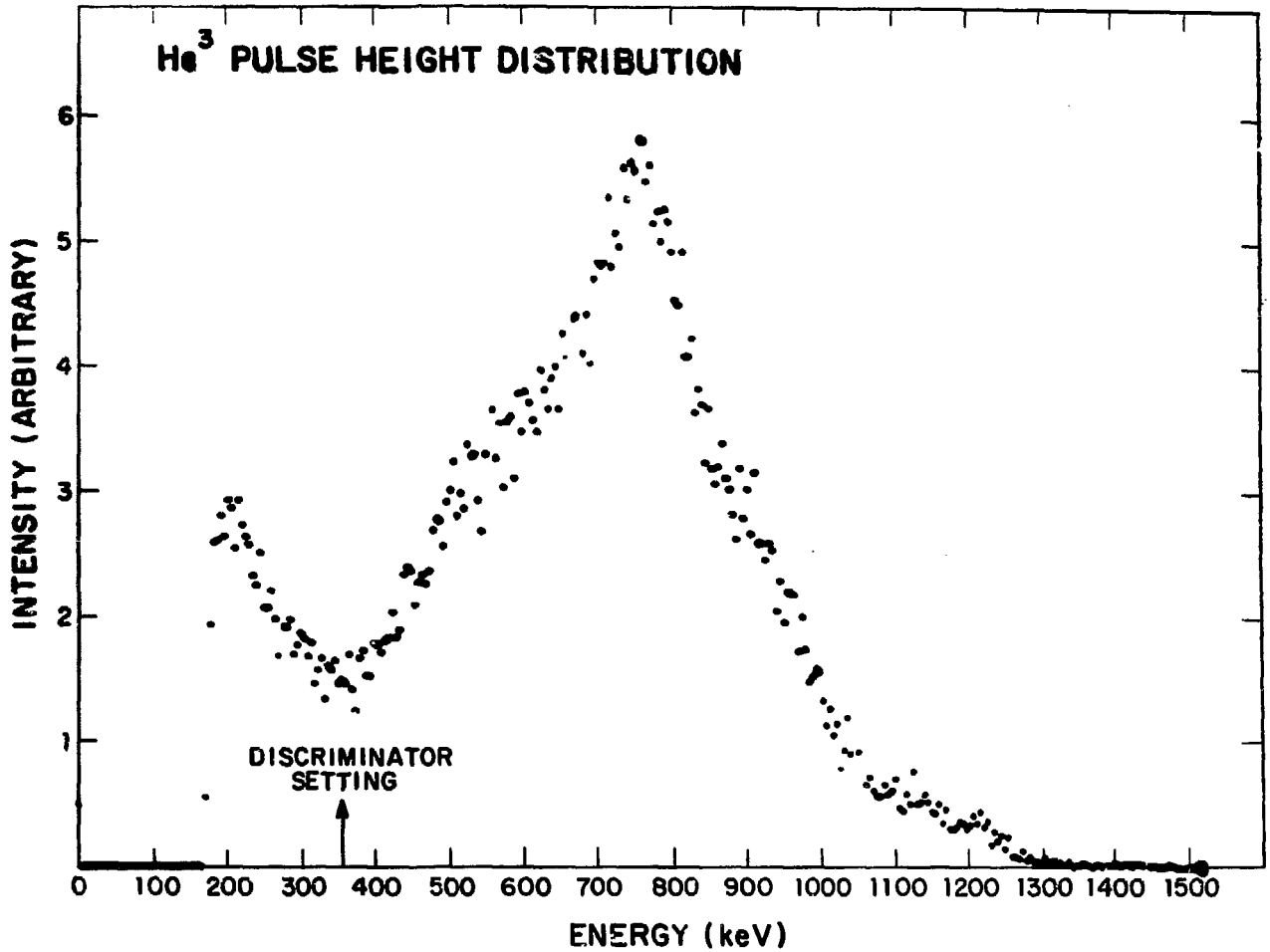
He³ PULSE HEIGHT DISTRIBUTION
INTENSITY (ARBITRARY)
1
2
3
4
5
6
DISCRIMINATOR SETTING
0
100
200
300
400
500
600
700
800
900
1000
1100
1200
1300
1400
1500
ENERGY (keV)

FIGURE 10

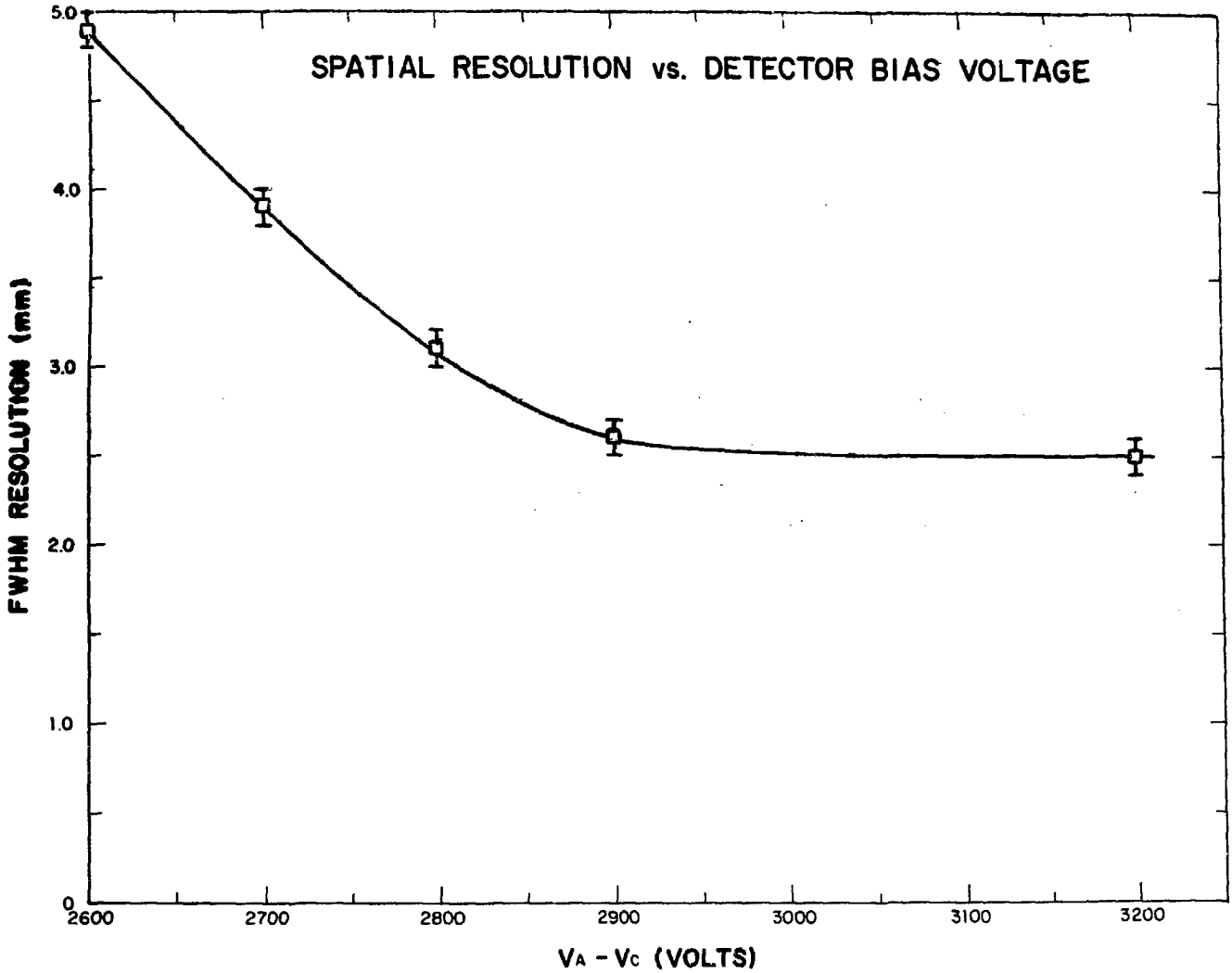
SPATIAL RESOLUTION vs. DETECTOR BIAS VOLTAGE
FWHM RESOLUTION (mm)
5.0
4.0
3.0
2.0
1.0
0
2600
2700
2800
2900
3000
3100
3200
VA - Vc (VOLTS)

FIGURE 11

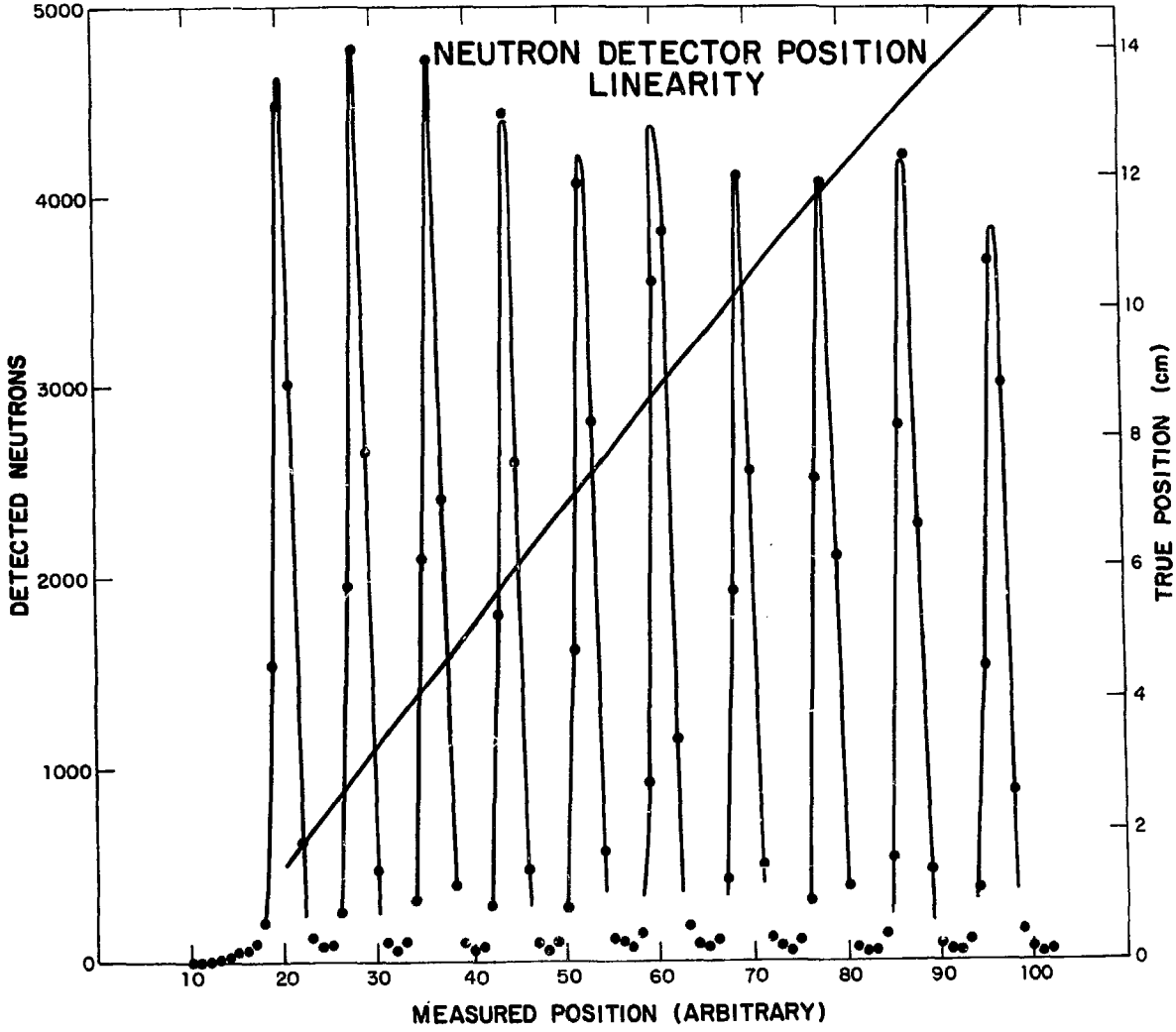
NEUTRON DETECTOR POSITION
LINEARITY
DETECTED NEUTRONS
TRUE POSITION (cm)
MEASURED POSITION (ARBITRARY)
5000
4000
3000
2000
1000
0
14
12
10
8
6
4
2
0
10
20
30
40
50
60
70
80
90
100

FIGURE 12

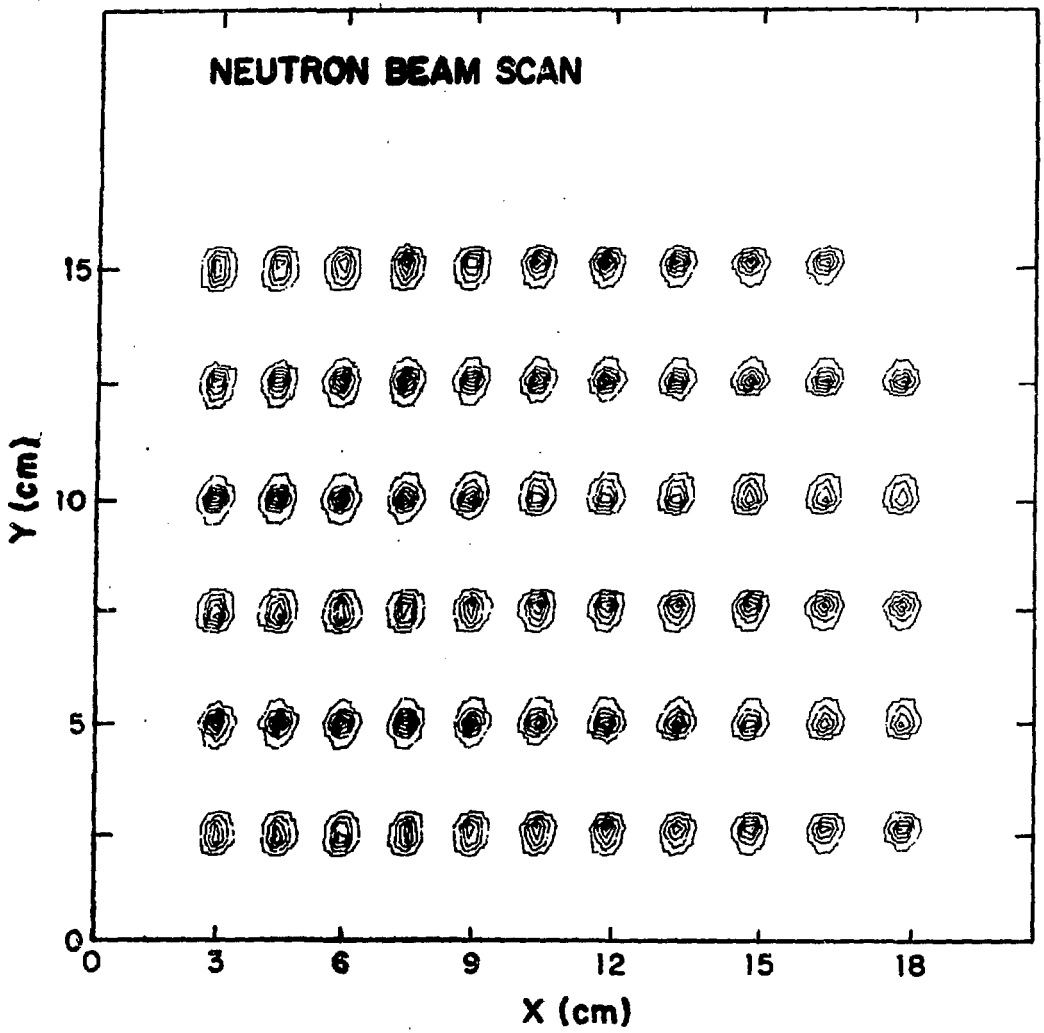

FIGURE 13

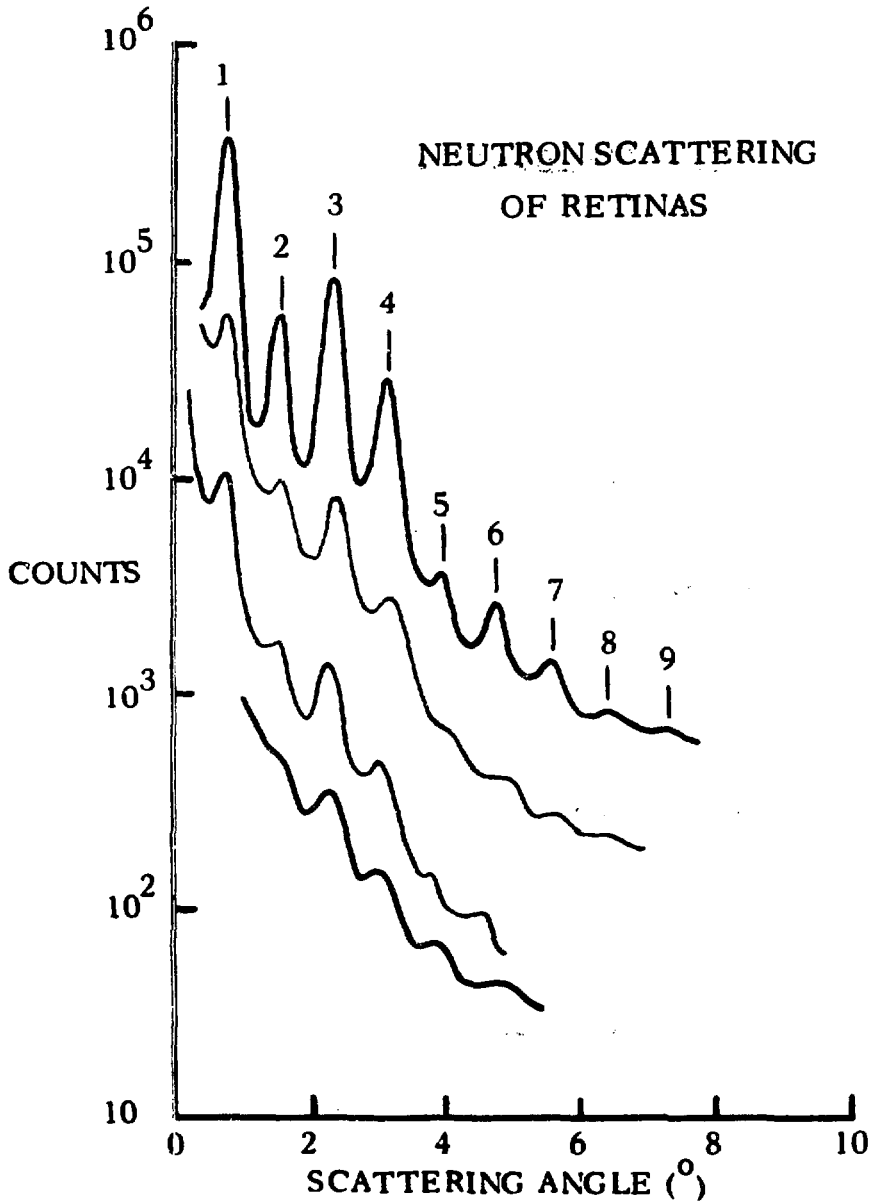
NEUTRON SCATTERING
OF RETINAS
COUNTS
SCATTERING ANGLE (°)
1
2
3
4
5
6
7
8
9
10^6
10^5
10^4
10^3
10^2
10
0
2
4
6
8
10

FIGURE 14